Carbon 229 (2024) 119455

Contents lists available at ScienceDirect

Carbon

journal homepage: www.elsevier.com/locate/carbon

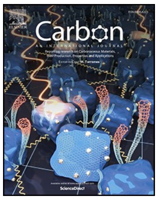

Simultaneous improvement in the elastic and fracture properties of graphene-epoxy nanocomposites–a computational perspective

Pritom Bose [a], Nikhil Koratkar [a,b,**], Yunfeng Shi [b,*]

[a] *Department of Mechanical, Aerospace and Nuclear Engineering, Rensselaer Polytechnic Institute, 110 8TH Street, Troy, NY, 12180, USA*
[b] *Department of Materials Science and Engineering, Rensselaer Polytechnic Institute, 110 8TH Street, Troy, NY, 12180, USA*

ARTICLE INFO

Keywords:
Graphene
Epoxy
Nanocomposites
Modulus
Strength
Toughness

ABSTRACT

The incorporation of stiff nano-additives (such as graphene) into a relatively soft polymer material (such as epoxy) usually leads to an improvement in elastic properties (i.e., Young's modulus) at the expense of fracture properties (i.e., tensile strength and toughness). Despite over a decade of research in polymer nanocomposites, we still lack a clear understanding of their structure-property relationships, which limits us from enhancing both elastic and fracture properties concurrently. Here, we performed large-scale reactive molecular dynamics simulations to study the deformation and fracture of model graphene/epoxy systems under uniaxial tension. A computationally efficient reactive force field was developed for graphene-epoxy system, allowing covalent bond formation, and breaking, which is crucial to model cross-linking in model epoxy as well as fracture. It was found the mechanical properties of the nanocomposite are very sensitive to the strength of the graphene-epoxy interface. As expected, elastic modulus increases with the interfacial strength. However, there appears to be an optimal interfacial strength to enhance the tensile strength and toughness. This is due to stress concentration occurring near the graphene edges at high interfacial strength, which leads to premature fracture. We show that by appropriately selecting an intermediate interface strength, one can simultaneously improve the ultimate tensile strength, toughness and the Young's modulus of the nanocomposite epoxy at ultra-low (~0.2 % by weight) loading fraction of graphene additives. Our findings highlight the critical importance of properly engineered additive-matrix interfacial strength to develop high-performing polymer nanocomposites that are concurrently stiff, strong as well as tough.

1. Introduction

Nanocomposite materials have one or more components with dimension(s) < 100 nm [1]. Usually, such nanometer-sized particulates or additives are dispersed into a host matrix to improve mechanical, thermal or electrical performance [2–5]. Due to their huge surface area to volume ratio, a trace amount of nano-particulates can significantly enhance the targeted material properties. The matrix material in nanocomposites can be polymers, metals or ceramics based on the intended application. Among polymers, epoxies are widely used in structural applications due to their superior stiffness, chemical inertness and high-temperature stability [6–10]. However, epoxy-based materials are generally brittle in nature, and hence it is important to improve their toughness and fracture strength without compromising on the stiffness.

Two-dimensional graphene materials are extraordinarily stiff and strong with a Young's modulus of ~1 TPa and ultimate tensile strength of ~130 GPa [11]. Graphene-based nanofillers can significantly improve the modulus of epoxy nanocomposites, even at a very low loading fraction. Indeed, there is a vast body of experimental literature [12–20] which indicates that graphene and graphene derivatives (such as reduced graphene oxide) are highly effective at enhancing the elastic properties (i.e., modulus). However, when it comes to the nanocomposite's fracture properties, the results are mixed: graphene-based nanofillers have been shown to either reduce [16,17,20–22] or enhance [12,14,15,18,19,23] the ultimate tensile strength and toughness. Given the variation in experimental test conditions (strain rate, temperature), epoxy chemistry and nanofiller (graphene) chemistry as well as materials processing conditions (such as graphene loading fraction, alignment, dispersion etc.), it is difficult to pinpoint the underlying reasons for the contradicting experimental results.

---

[*] Corresponding author.
[**] Corresponding author. Department of Mechanical, Aerospace and Nuclear Engineering, Rensselaer Polytechnic Institute, 110 8TH Street, Troy, NY, 12180, USA.
E-mail addresses: koratn@rpi.edu (N. Koratkar), shiy2@rpi.edu (Y. Shi).

https://doi.org/10.1016/j.carbon.2024.119455
Received 9 May 2024; Received in revised form 1 July 2024; Accepted 18 July 2024

As opposed to experiments, molecular dynamics (MD) simulations of graphene/epoxy model systems can help understand the filler/polymer interaction [24,25] and the deformation mechanism at the molecular-level, while precisely controlling the chemistry, processing and testing conditions. However, MD simulations on fracture response of epoxy systems have proven to be challenging. For instance, experimental epoxy materials are generally brittle and fail within 10 % tensile strain. Yet, the current literature [26–34] on MD modeling of epoxies generally show highly ductile behavior showing failure occurring at 100–500 % tensile strain. Such artificial ductility observed in simulations could arise from sample size effect, high strain rate, or both. The force field used to model fracture behavior of polymeric nanocomposites must be able to describe covalent bond breaking and formation, which is generally termed as reactive potential. To this end, most existing reactive potentials are computationally too expensive to handle systems that are large enough in size to avoid the sample size effect [35–40]. Although, in practice epoxy composites are brittle in nature, the current literature is significantly limited to very ductile samples partly because of the computational demand with conventional interatomic potentials. This is problematic since fracture and toughening mechanism(s) are expected to be vastly different for inherently brittle materials such as epoxies. Moreover, brittle fractures are inherently stochastic, and it is particularly difficult to predict the fracture when the system has inhomogeneities, for example a nano-additive in the matrix. To establish a quantitative and statistical understanding of the nanocomposite one must carefully examine sample-to-sample variations which is also prohibitive for such expensive potentials. Therefore, simplified polymer nanocomposite models capable of describing chemical reactions are better suited for modeling reliable fracture behaviors of these materials.

In this study, we have developed a coarse-grained molecular model of epoxy-polymer/graphene and a simple pairwise reactive potential to run MD simulations with high computational efficiency. Consistent with experimental observation, neat epoxy sample exhibits brittle fracture in our MD simulations. Furthermore, it was found that the graphene/epoxy interface interaction plays a “pivotal role” in modulating the elastic and fracture properties of the nanocomposite. We show that by proper tailoring of the interface interaction one can indeed achieve a concurrent increase in both elastic and fracture properties.

2. Methods

We constructed a reactive coarse-grained particle-based model system to describe epoxy-graphene nanocomposites, including epoxy linear polymer chains, cross-linkers, and graphene. More importantly, the reactive force field used here is capable of stabilizing the said molecular structures and describing the cross-linking reaction, as well as bond rupturing during tensile tests. There are five types of particles (see Fig. 1) in our modeling approach: P_A, P_B, L, C_A and C_B. P_A, P_B represent monomers constituting the linear polymer chain, L is the crosslinking agent, C_A, C_B are carbon particles in graphene.

Interaction parameters between different particle species are described using a modified Lennard Jones potential (see discussion below). We tuned the parameters to reproduce literature values of various material properties as shown in Table 1.

The particle-particle interaction is described by a modified Lennard-Jones (mLJ) potential:

$$\phi_{LJ}(r) = 4\varepsilon_{\alpha\beta}\left(\frac{\sigma_{\alpha\beta}^{12}}{r^{12}} - \frac{\sigma_{\alpha\beta}^{6}}{r^{6}}\right) - 4\varepsilon_{\alpha\beta}\left(\frac{\sigma_{\alpha\beta}^{12}}{r_{\alpha\beta,c}^{12}} - \frac{\sigma_{\alpha\beta}^{6}}{r_{\alpha\beta,c}^{6}}\right)\phi_{mLJ}(r)$$

$$\phi_{mLJ}(r) = \begin{cases} \phi_{LJ}(r), r < r_{\alpha\beta,s} \\ \phi_{LJ}(r) + \varepsilon_B\varepsilon_{\alpha\beta} \bullet \sin^2\left(\pi\frac{r_{\alpha\beta,c} - r}{r_{\alpha\beta,c} - r_{\alpha\beta,s}}\right), r_{\alpha\beta,s} \le r < r_{\alpha\beta,e} \\ \phi_{LJ}(r), r > r_{\alpha\beta,e} \end{cases}$$

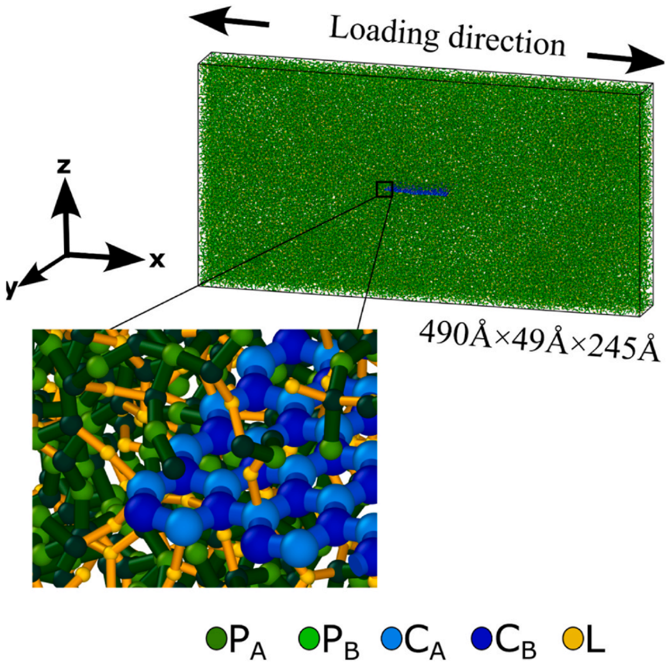

Fig. 1. Coarse-grained epoxy nanocomposite model consists of linear chains (dark and light green), curing agent (orange), and graphene (dark and light blue). A close-up view near the graphene-polymer interface is presented. (A colour version of this figure can be viewed online.)

Table 1
Comparison of various material properties in literature and in our simulation.

Material Property	Values in literature	In our simulation
Flexural rigidity of graphene	3.9 eV Å^2 [41]	3.9 eV•- Å^2
Young’s modulus of graphene	1.0 TPa [11]	1.0 TPa
Young’s modulus of hardened Epoxy	0.9–3.95 GPa [12,42] [45]	1.8 GPa
Areal density of graphene	4.58 (g/mol)/Å^2 [46]	4.58 (g/mol)/Å^2
Density of Epoxy (crosslinked)	1.15–1.2 g/cc [12,44]	1.15 g/cc
Tensile strength of graphene (armchair)	53 GPa, Experimental [47], ~130 GPa, theoretical [47, 48]	115 GPa

Here, $\phi_{LJ}(r)$ is the conventional truncated LJ potential. α, β denotes two particle species, respectively with $\varepsilon_{\alpha\beta}$ and $\sigma_{\alpha\beta}$ providing the energy and length scales and $r_{\alpha\beta,c}$ providing the cutoff. $\phi_{mLJ}(r)$ includes an additional energy penalty term between $r_{\alpha\beta,s}$ and $r_{\alpha\beta,e}$ with a bump height of $\varepsilon_B\varepsilon_{\alpha\beta}$. The potential parameters are indicated in Table 2. We used an internal unit system in LAMMPS [47]. The length, mass and energy units

Table 2
List of potential parameters used in our simulations.

Interaction type	$\varepsilon_{\alpha\beta}/\varepsilon_0$	$\sigma_{\alpha\beta}/\sigma_0$	$r_{\alpha\beta,s}/\sigma_0$	$r_{\alpha\beta,e}/r_{\alpha\beta,c}$	$\varepsilon_B/\varepsilon_0$	$r_{\alpha\beta,c}$ (Å)
P_A-P_B	0.1	1.0	1.2	1.0	4.5	2.58
P_A-P_A	0.01	2.1	1.0	0.0	0.0	4.11
C_A-C_B	20	1.0	1.13	1.0	1.0	2.41
C_A-C_A	0.10	2.2	1.0	1.0	0.0	4.11
L-P_A (reactive)	2.0	1.0	1.2	1.0	0.6	2.41
L-P_A (non-reactive)	0.01	2.0	0.0	1.0	0.0	2.84
L-P_B	0.01	2.0	0.0	0.0	0.0	2.84
P_A or P_B vs C_A or C_B	0.1	2.1	0.0	0.0	0.0	4.11
L-C_A	Variable	1.175	1.2	1.0	0.0	3.12

were chosen as follows to best match experimental values as shown in Table 1: $\sigma_0 = 1.42$ Å, $m_0 = 1.31$ *a.m.u.* and $\varepsilon_0 = 0.55$ eV (see **method of calculation** and Fig. S1 in the supplementary information).

Mass values of P_A, P_B and L particles are set to 15.0 m_0 to reproduce a realistic neat epoxy density of 1.15 g/cc. C_A, C_B mass are set to 9.16 m_0. Crosslinking and annealing temperatures are fixed to 1100K and 70K. We set the crosslinking temperature to be very high to promote an accelerated reaction and enhanced configuration exploration. During high temperature crosslinking, we increased the potential depth between P_A-P_B to preserve the topology of the linear polymer. The numerical integration timestep was set as 0.112 fs.

The epoxy linear polymer chains were constructed by alternating P_A and P_B particles, with strong P_A-P_B attraction yet with strong P_A-P_A and P_B-P_B repulsion. The range of such repulsion was chosen to prevent over-coordination of more than two to maintain bi-functional topology. This strategy has been used in our previous works [48–50] on modeling various polymeric systems. The model epoxy linear chains are mono-dispersed with 151 particles (76 P_A and 75 P_B). The linker particles (L particles) preferentially bind to P_A particles over P_B particles, while have repulsive-only interaction with all other particles. In this way, cross-linking can be established between two epoxy chains, bridged by one L particle as P_A (belong to one chain)-L-P_A (belong to another chain). The formation of L-P_A bonding must overcome a potential barrier, which effectively controls the crosslinking rate of model epoxy. The model graphene flake was constructed by particles C_A and C_B, with strong C_A-C_B attraction yet with strong C_A-C_A and C_B-C_B repulsion. The range of such repulsion was chosen to prevent over-coordination of more than three to stabilize the graphene structure.

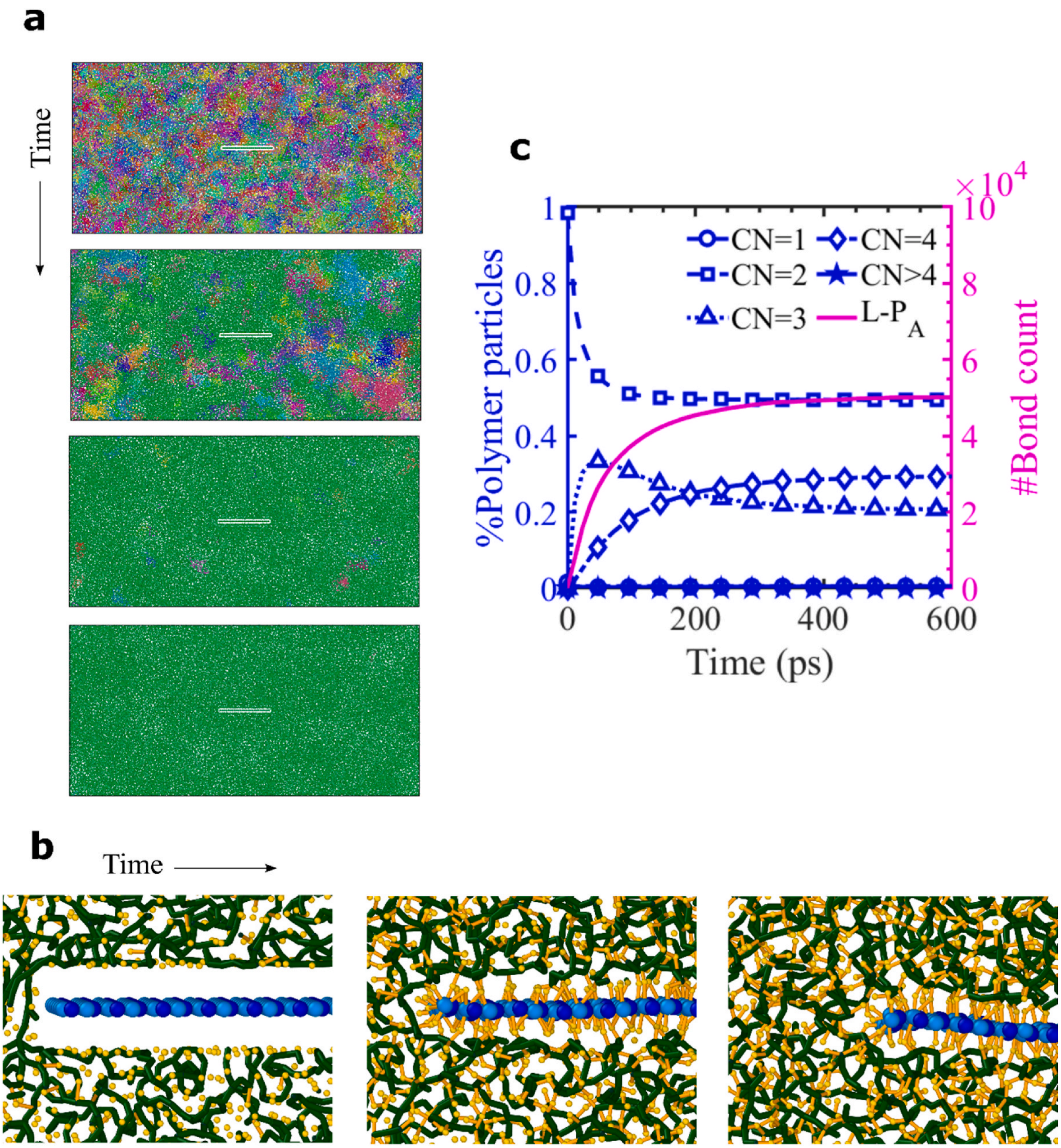

Fig. 2. Crosslinking reaction with time. (a) cluster analysis with OVITO [51] reveals the percolation of the polymer chains with time. Each cluster is uniquely colored. (b) Crosslinking with time (0ps, 60ps and 600 ps from left to right). (c) Percentage of polymer particles with coordination number (CN) 1 to 4 and above (left Y axis). Initially all the polymer particles (except the ends) have a coordination number of 2. Total number of bonds in the system (right Y-axis). (A colour version of this figure can be viewed online.)

The model nanocomposite samples are in a thin-slab geometry (as shown in Fig. 1) to maximize the size of the simulation system in two out of three directions. All three directions are subjected to periodic boundary conditions to simulate bulk properties. To prepare the nanocomposite sample, we first started with a dilute random distribution of polymer chains with uniform chain length, dispersed with L linker particles at a density of 94 μg/cc at a temperature of 70 K. It should be noted that the L-P_A bonding is switched off (that is, identical to L-P_B) so that crosslinking reaction will not interfere with epoxy chain relaxation. The simulation box is isothermally and hydrostatically compressed to generate a compact polymer nanocomposite retaining the random orientations. During hydro-compression, a rectangular region of 7 nm by 0.8 nm with repulsive wall is maintained in the simulation box as a spacer to insert graphene later. The purpose of initiating with a very low-density polymer and the hydrostatic compression thereafter is to attain an isotropic epoxy sample. The system was further relaxed in NVT ensemble at $T_{high} = 1100$ K for 0.3 ns. During high temperature relaxation, intra chain bond breaking is prevented by increasing the energy bump height between P_A and P_B. Next, the graphene was inserted into the spacer region, and the L-P_A bonding was turned on to allow crosslinking reaction to occur at T_{high} for 0.6 ns, which is sufficiently long for the saturation of the crosslinking reaction. Details can be found in the next section. Before mechanical testing, the sample was relaxed in NPT to zero stress, at which point the density of the polymer is ~1.15 g/cc.

3. Results and discussion

3.1. Crosslinking process

Fig. 2 shows the process of the crosslinking reaction at the molecular level at 1100 K. The coordination number of P_A polymer particles can be used to monitor the progression of the crosslinking reaction. The cutoff for calculating the coordination number was chosen to be 2.41 Å, which corresponds to the potential cutoff for L-P_A bonds. As shown in Fig. 2c, the number of L-P_A bonds increases and then saturates over time. It should be noted that a high curing temperature was chosen to speed up the reaction. A simple estimation based on a reaction barrier, estimated from the L-P_A pair interaction, of 0.57 eV (54.8 kJ/mol) means 500 ps curing at 1100 K is equivalent to about 4.4 ms of curing at 300 K ($\sim 10^7$ speed up). For reference, experimentally and DFT calculated activation energies for similar polymerization reactions are 50–74 kJ/mol [52,53] and 71–94 kJ/mol [54] respectively.

At the initial stage, all chains are linear, and all the polymer atoms, P_A and P_B (except at the ends) hold a coordination of 2. Due to the abundance of reactive monomers and reagent molecules, the reaction rate is highest in the beginning. During crosslinking reactions, intra-chain and inter-chain links are formed via the linker groups. Doubly coordinated polymer atoms become three and four-coordinated. As the reaction progresses, the reaction rate goes down and eventually gets saturated. We observe that at saturation, ~30 % of polymer particles become 4-coordinated, ~20 % 3-coordinated and ~50 % remain 2-coordinated. At the end, steric hindrance causes the reaction to slow down indefinitely before saturating all the active sites.

We also investigated the mechanical responses of epoxy samples at different stages (i.e., different crosslinking times) of the crosslinking process. Model epoxies with different degrees of crosslinking were cooled down, with residual stress relaxed, and then subjected to uniaxial tensile tests. These simulated mechanical tests were performed at 70K and at a strain rate of 2.3×10^8 s^{-1}. As the extent of crosslinking increases, a ductile-to-brittle transition is evident as shown in Fig. 3a. The

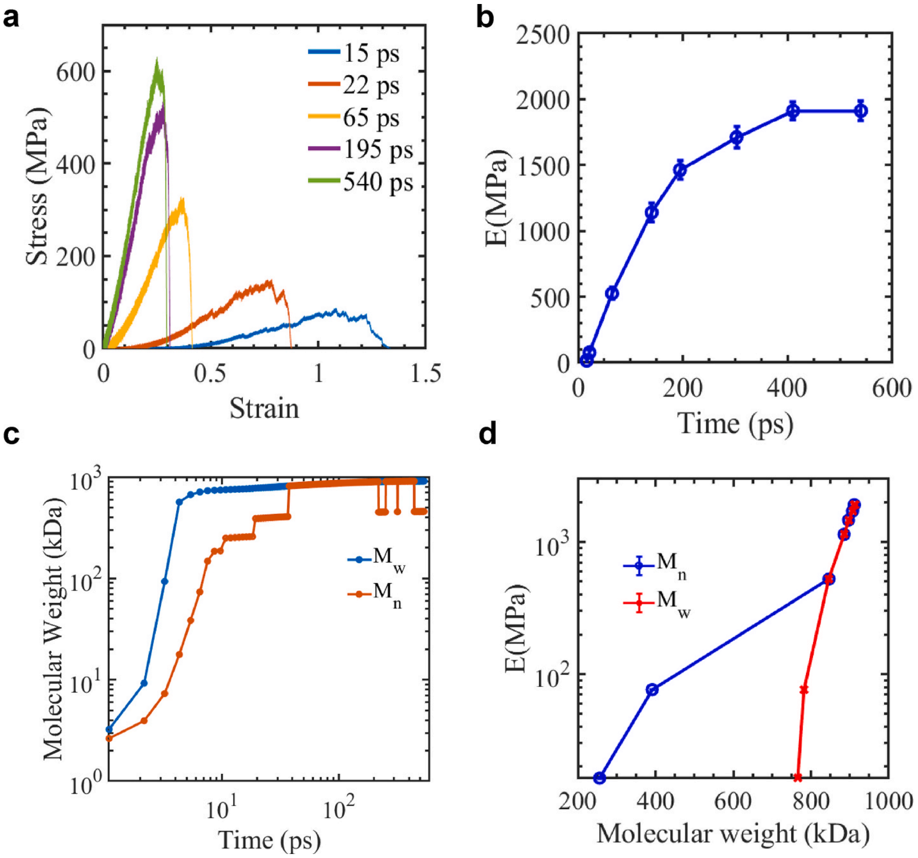

Fig. 3. (a) Stress-Strain curve for mechanical testing of neat epoxy after different crosslinking duration. (b) Elastic modulus of neat epoxy with crosslinking duration. (c) Number-average (M_n) and weight-average (M_w) molecular weight of the epoxy as a function of curing time during crosslinking. (d) Young's modulus of crosslinked epoxy as a function of M_w and M_n. (A colour version of this figure can be viewed online.)

Young's modulus of the samples with respect to their crosslinking duration is shown in Fig. 3b. The observed curing vs Young's modulus increase agrees well with the experimental results by Lindorse [55]. In addition, weight-average and number-average molecular weight distribution (M_w and M_n) have been plotted with time (Fig. 3c). M_w grows faster and reaches a plateau earlier than M_n. It signifies that larger clusters start to form once crosslinking initiates. The number of larger clusters becomes stable quickly while the smaller clusters keep forming and stitching the larger clusters together to ultimately connect the whole system at around 37 ps, when M_n equals to M_w. As shown in Fig. 3d, the Young's modulus of the crosslinked epoxy strongly correlates to the molecular weight. The final crosslinked neat epoxy (with crosslinking duration of ~540 ps) has a Young's modulus of ~1800 MPa and, density of ~1.15 g/cc, consistent with experimental values [12,42–45].

3.2. System size effect

Mechanical tests on nanometer-sized samples in molecular-level simulation often are subjected to various size effects. For brittle fracture, the sample must possess enough strain energy to drive crack formation from the energy point of view. This simple Griffith-type of consideration leads to a critical sample length, below which the sample is more ductile relative to longer samples [56,57]. To investigate the proper sample size, three epoxy samples of different sizes were prepared and tested: 1×, 4× and 16× systems have simulation box lengths of 245 Å, 490 Å and 980 Å respectively along the loading direction (Fig. 4). It is clear that the smallest system fails at a larger strain. However, for both 4× and 16× systems, we observed similar failure strain, which suggests that the 4× system was free of artificial ductility effects and was therefore used for the simulation results shown in Figs. 5–7.

3.3. Strain rate effect

Strain rate is another key factor that could significantly affect the mechanical behavior of materials. Increased strength at high strain rate was previously been reported [58] for polymer molecular simulations. To investigate the strain rate effect, we applied loading at four different strain rates (s^{-1}): 4.6×10^7, 2.3×10^8, 4.6×10^8 and 2.3×10^9. Our results (Fig. 5) indicate that the fastest strain rate (2.3×10^9 s^{-1}) induces a spurious toughening effect. This specific loading case shows both a higher failure strength and a higher failure strain. We see that all the other test cases fail at a similar failure strain (Fig. 5). Although the slowest strain rate (4.6×10^7 s^{-1}) simulation shows a smaller failure strength, it has a similar failure strain and comparable toughness with the 2.3×10^8 s^{-1} and 4.6×10^8 s^{-1} cases. In all subsequent simulations (Figs. 6–7), we load our samples at a fixed 2.3×10^8 s^{-1} strain rate.

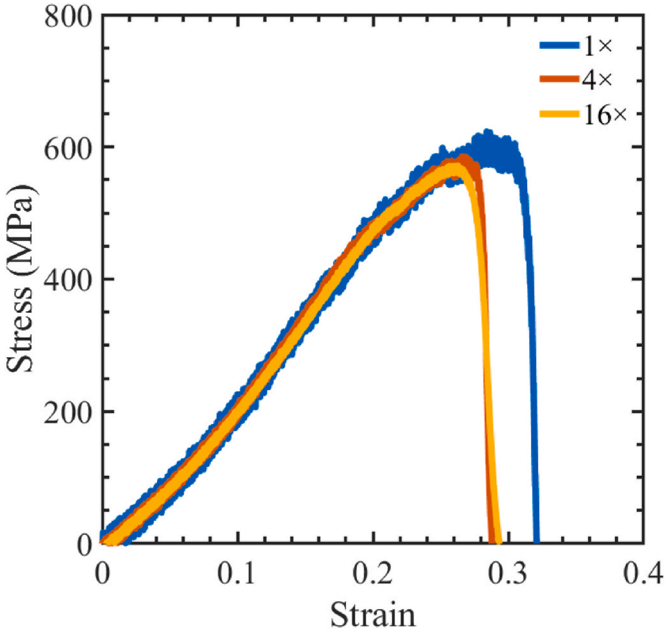

Fig. 4. Stress-strain response in uniaxial tension test in neat epoxy samples showing size effect. 1 × , 4 × and 16 × samples have simulation box lengths of 245 Å, 490 Å and 980 Å (320,1280 and 5120 chains) respectively. (A colour version of this figure can be viewed online.)

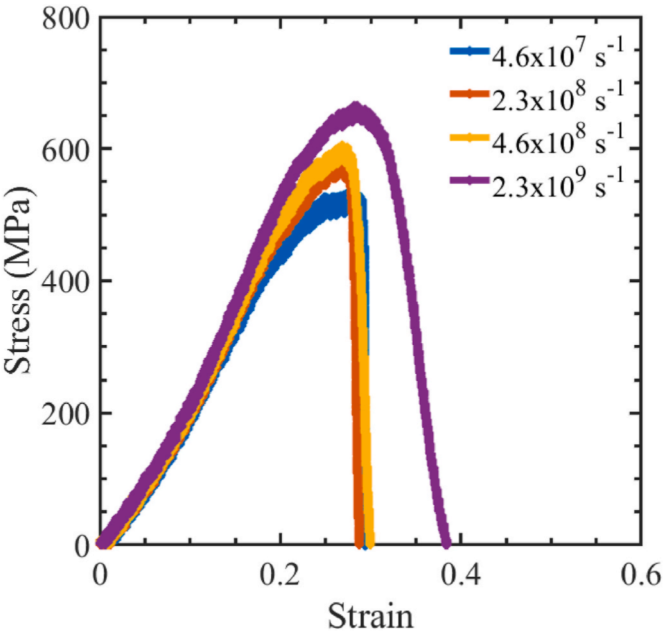

Fig. 5. Stress-strain response in uniaxial tension test in neat epoxy samples showing strain rate effect. (A colour version of this figure can be viewed online.)

3.4. Nanocomposite mechanical properties: effect of polymer/graphene interface

Chemically modified graphene surfaces with functional groups (FG) can form covalent bonds with neighboring polymer chains. Previous experimental study [59] shows that interface covalent bonding might be crucial to improve the mechanical response of epoxy nano-composites. Here, we focused on nanocomposite with one single graphene inclusion (~0.2 wt% in a 490 Å × 245 Å × 49 Å epoxy system) that is oriented parallelly to the uniaxial tensile direction, to illustrate the effect of graphene-epoxy interface. This orientation was selected to minimize the obvious crack opening effect at low interface bonding. To regulate the interface strength, we control the interface potential depth (see Fig. S2) during crosslinking. Since brittle fracture is a random process, we simulated 20 independent samples for seven distinct cases-neat epoxy and six nanocomposites with increasing interfacial strength (5–150 eV/Å^2) denoted as FG-1 to FG-6. This is to better understand the failure mechanism behind the stochastic failure behavior and quantify mechanical properties with uncertainty. Each independent sample is separately prepared from independent initial configurations yet with the identical processing procedure.

To study the effect of graphene/epoxy interface strength, we performed simulated uniaxial tensile loading tests (along the x direction) on the nanocomposite samples of varied interfacial strength and compared them with the neat (pure) epoxy sample (Fig. 6). In our model, pure epoxy has a Young's modulus of ~1812 MPa. We observe that adding ~0.2 wt% of graphene sheet increases the modulus of the neat epoxy by 25–33 % depending on the interfacial strength. When the interface is

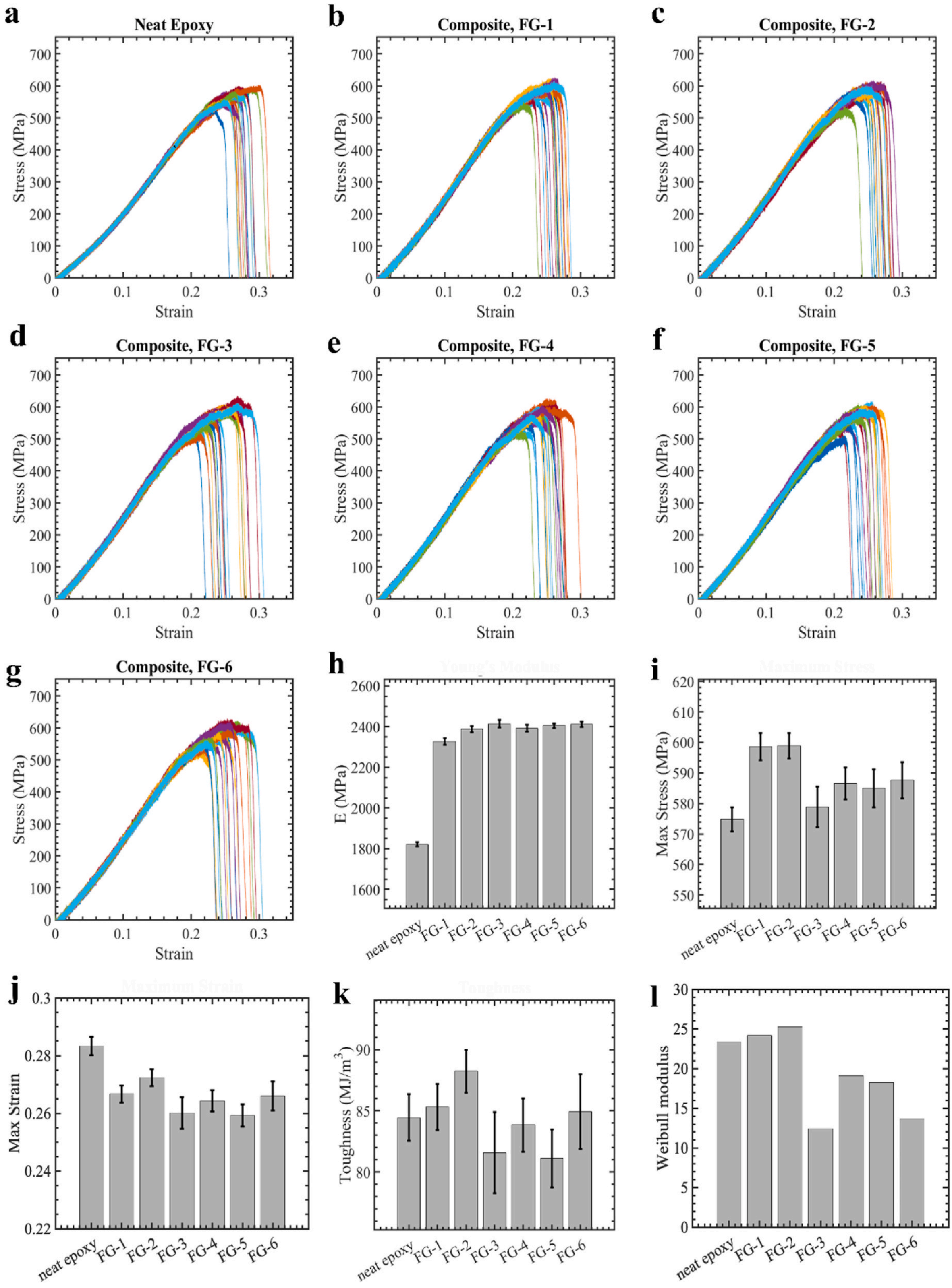

Fig. 6. Interfacial strength effect on the mechanical properties of a 0.2 wt% graphene/epoxy nanocomposite. (a–g) Simulated stress strain curves for neat epoxy and nanocomposites, each with 20 independent samples. (h–l) Various mechanical properties. (A colour version of this figure can be viewed online.)

stronger, the stiffer interface bonds lead to a noticeable stiffening effect on the composite. Even at the lowest interfacial strength, there is an appreciable increase in Young's modulus from the neat epoxy samples due to the presence of the graphene flake. However, the young's modulus increase may be slightly overestimated due to transverse stiffness of graphene in the slab geometry. Tensile strength and toughness were also found to be improved with interfacial strength up to FG-2 where we observed a ~4.2 % increase in tensile strength and ~4.5 % increase in toughness.

As the interface becomes stronger, we see an interesting pattern in

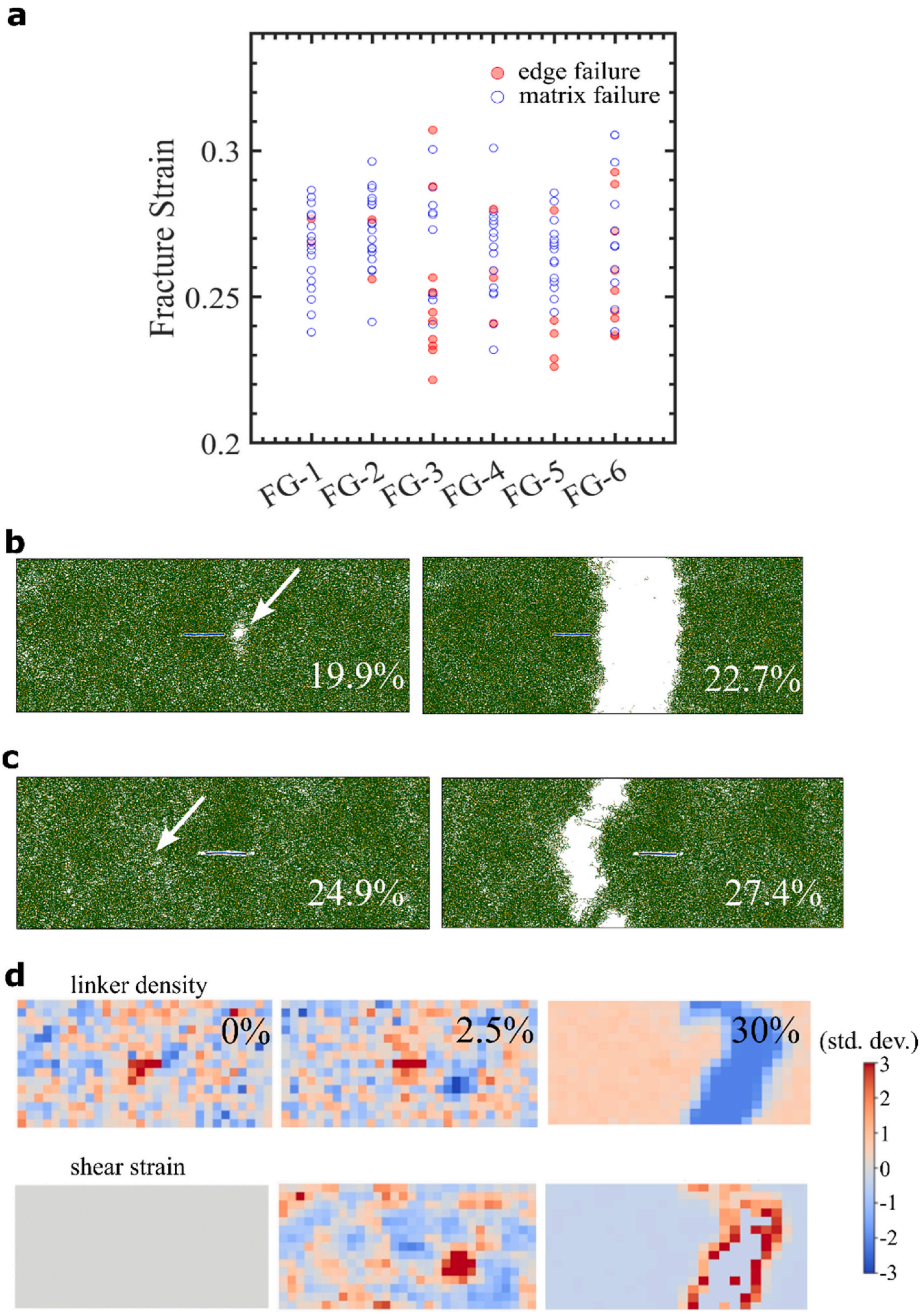

Fig. 7. (a) Failure mode analysis. Edge cavitation is common in premature failure. Stronger interfaces tend to cavitate and fail through the edge more often. (b) Typical edge failure starts with a cavity formation near the filler/matrix interface and quickly propagates as a crack. (c) Typical matrix failure. The white arrows dictate the initial positions of failure. (d) Mean normalized linker density and shear strain map. Units are in standard deviations of the respective frames. (A colour version of this figure can be viewed online.)

the average values of ultimate tensile strength and toughness (Fig. 6). Both the toughness and the ultimate strength peak at FG-2 which is a "semi-strong" interface. In this study, graphene fibers are stiffer than the surrounding polymer matrix and are aligned with the direction of the applied load. As a result, the polymer adjacent to the graphene basal plane near the center does not experience the global strain as much due to inadequate local straining and is subjected to mild compressive stress. Therefore, during uniaxial tensile strain, the edge bonds are stretched rather than the planar bonds.

If the interface between graphene and polymer is excessively strong (FG-3 or higher), the anchoring bonds are unable to stretch sufficiently while the adjacent polymer chains attempt to align with the global strain. To maintain compatibility in strain, the local stress distribution is modified eventually leading to cavitation near the graphene edges, as shown in Fig. 7b. Edge cavitation is the dominant mode for premature failure observed for strong interfaces, arising due to elevated stress concentration (see Fig. 7a). About 65 % of the least five ductile samples for FG-3,4,5 and 6 fail from the graphene edges where only about 10 % of the least five ductile samples for FG-1 and 2 fail from edges. This behavior results in a wide variability in failure strain for FG-3 which corresponds to the shift from matrix failure to edge failure and translates to a lower Weibull modulus (Fig. 6l).

For samples with interfacial strength below a strength threshold (FG-3), the tendency for edge cavitation falls sharply. We analyzed all 20 samples for FG-3 composite. We chose FG-3 because it has the widest variation of failure strain among all the categories. The most ductile sample sustains over 30.5 % strain while the least ductile sample fails at 22 % strain. One representative case is shown in Fig. 7c. We identified a possible reason for such wide variability of mechanical performance. All our highly crosslinked polymer samples are prepared from a homogenous distribution of crosslinkers; however, local inhomogeneity is unavoidable due to the steric effect. Local inhomogeneity of polymer connectivity can be visualized from the distribution of linker groups. First row in Fig. 7d shows 2D histogram of linker distribution where the linker atoms have a coordination number of 2 or more and the second row shows corresponding relative atomic shear strain, ε_{xz}. Both the linker distribution and the atomic shear strain were zero mean standardized before presenting. We observe that local lack of connectivity (soft spots) correlates with an elevated local shear strain. Fig. S3 show an inverse linear correlation between connectivity and shear strain, especially near their extrema. These soft spots are stable and maintain locality at the beginning but at sufficient strain, grow and interact with each other and eventually create cracks. Complex interactions between these soft spots and the effect of stress on these items are out of the scope of this paper (see Ref. [60] for further reading on material soft spots). During the crack growth process, the soft spots act as an additional mode for energy expenditure and increase the ductility.

To summarize, we observe that samples with higher ductility more often fail through shear activity in the matrix than from the filler/matrix interface and these shear spots usually correlate with the inhomogeneity in polymer crosslinking. On the other hand, highly brittle samples usually fail from cavitation that appears near the filler/matrix interface. Premature failure from cavitation is statistically significant for the stronger interfaces which is expected due to elevated stress concentration. When two modes are both active, as in the case of FG-3, the fluctuation in mechanical properties reaches maximum.

4. Conclusion

In this study, we used molecular dynamics simulations to investigate the mechanical properties of a brittle graphene/epoxy nanocomposite system at an ultra-low graphene loading condition (~0.2 wt%). Our approach featured a two-body reactive potential (bump LJ potential) that can efficiently simulate bond breaking/formation in a large polymer system with a comparatively smaller amount of computing resources. Our findings reveal that advantageous mechanical properties are achieved not at the strongest graphene/epoxy interface but at moderate strengths. At the optimal level of interfacial strength, Young's modulus increased by ~33 % while tensile strength and toughness increased by ~4.2 % and ~4.5 % respectively, compared to the neat epoxy. We observed that overly strong interfaces led to a significant increase in edge cavitation and premature failure, with as much as 65 % of the least ductile samples failing through edge cavitation near the graphene edges. In contrast, weaker interfaces reduced such failures to about 10 %. Our simulations underscore the importance of carefully balancing the interfacial strength to simultaneously enhance stiffness, strength, toughness, and durability in nanocomposites, providing crucial insights for designing high-performance materials for structural applications.

CRediT authorship contribution statement

Pritom Bose: Writing – original draft, Formal analysis, Data curation, Conceptualization. **Nikhil Koratkar:** Writing – original draft, Supervision, Project administration, Methodology, Investigation, Funding acquisition, Formal analysis, Conceptualization. **Yunfeng Shi:** Writing – original draft, Supervision, Methodology, Investigation, Formal analysis, Data curation, Conceptualization.

Declaration of competing interest

The authors declare that they have no known competing financial interests or personal relationships that could have appeared to influence the work reported in this paper.

Acknowledgements

We acknowledge funding support from the USA National Science Foundation (Award 2015750). We thank the Center for Computational Innovations at RPI for providing computational facilities. NK also acknowledges support from the John A. Clark and Edward T. Crossan Chair Professorship at the Rensselaer Polytechnic Institute.

Appendix A. Supplementary data

Supplementary data to this article can be found online at https://doi.org/10.1016/j.carbon.2024.119455.

References

[1] A. Bielinska, J.D. Eichman, I. Lee, J.R. Baker, L. Balogh, Imaging {Au0-PAMAM} gold-dendrimer nanocomposites in cells, J. Nanoparticle Res. 4 (2002) 395–403, https://doi.org/10.1023/A:1021692006589.

[2] K.M.F. Shahil, A.A. Balandin, Graphene–multilayer graphene nanocomposites as highly efficient thermal interface materials, Nano Lett. 12 (2012) 861–867, https://doi.org/10.1021/nl203906r.

[3] G. Lalwani, A.M. Henslee, B. Farshid, L. Lin, F.K. Kasper, Y.-X. Qin, A.G. Mikos, B. Sitharaman, Two-dimensional nanostructure-reinforced biodegradable polymeric nanocomposites for bone tissue engineering, Biomacromolecules 14 (2013) 900–909, https://doi.org/10.1021/bm301995s.

[4] A.S. Wajid, H.S.T. Ahmed, S. Das, F. Irin, A.F. Jankowski, M.J. Green, High-performance pristine graphene/epoxy composites with enhanced mechanical and electrical properties, Macromol. Mater. Eng. 298 (2013) 339–347, https://doi.org/10.1002/mame.201200043.

[5] K. Hu, D.D. Kulkarni, I. Choi, V.V. Tsukruk, Graphene-polymer nanocomposites for structural and functional applications, Prog. Polym. Sci. 39 (2014) 1934–1972, https://doi.org/10.1016/j.progpolymsci.2014.03.001.

[6] A. Zandiatashbar, C.R. Picu, N. Koratkar, Control of epoxy creep using graphene, Small 8 (2012) 1676–1682, https://doi.org/10.1002/smll.201102686.

[7] S. Paolillo, Stefano Paolillo, R.K. Bose, M. Hernández, M.H. Santana, A.M. Grande, Intrinsic self-healing epoxies in polymer matrix composites (PMCs) for aerospace applications, Polymers 13 (2021) 1–32, https://doi.org/10.3390/polym13020201.

[8] A. Shundo, S. Yamamoto, K. Tanaka, Network Formation and physical properties of epoxy resins for future practical applications, JACS Au 2 (2022) 1522–1542, https://doi.org/10.1021/jacsau.2c00120.

[9] H. Gu, C. Ma, J. Gu, J. Guo, X. Yan, J. Huang, Q. Zhang, Z. Guo, An overview of multifunctional epoxy nanocomposites, J. Mater. Chem. C 4 (2016) 5890–5906, https://doi.org/10.1039/c6tc01210h.

[10] I. Srivastava, R.J. Mehta, Z.-Z. Yu, L. Schadler, N. Koratkar, Raman study of interfacial load transfer in graphene nanocomposites, Appl. Phys. Lett. 98 (2011) 063102, https://doi.org/10.1063/1.3552685.

[11] C. Lee, X. Wei, J.W. Kysar, J. Hone, Measurement of the elastic properties and intrinsic strength of monolayer graphene, Science 321 (2008) 385–388, https://doi.org/10.1126/science.1157996.

[12] M.A. Rafiee, J. Rafiee, Z. Wang, H. Song, Z.-Z. Yu, N. Koratkar, Enhanced mechanical properties of nanocomposites at low graphene content, ACS Nano 3 (2009) 3884–3890, https://doi.org/10.1021/nn9010472.

[13] J. Zhu, J. Kim, H. Peng, J.L. Margrave, V.N. Khabashesku, E.V. Barrera, Improving the dispersion and integration of single-walled carbon nanotubes in epoxy composites through functionalization, Nano Lett. 3 (2003) 1107–1113, https://doi.org/10.1021/nl0342489.

[14] T. Ramanathan, A.A. Abdala, S. Stankovich, D.A. Dikin, M. Herrera-Alonso, R. D. Piner, D.H. Adamson, H.C. Schniepp, X. Chen, R.S. Ruoff, S.T. Nguyen, I. A. Aksay, R.K. Prud'Homme, L.C. Brinson, Functionalized graphene sheets for polymer nanocomposites, Nat. Nanotechnol. 3 (2008) 327–331, https://doi.org/10.1038/nnano.2008.96.

[15] I. Zaman, T.T. Phan, H.-C. Kuan, Q. Meng, L.T. Bao La, L. Luong, O. Youssf, J. Ma, Epoxy/graphene platelets nanocomposites with two levels of interface strength, Polymer 52 (2011) 1603–1611, https://doi.org/10.1016/j.polymer.2011.02.003.

[16] J.A. King, D.R. Klimek, I. Miskioglu, G.M. Odegard, Mechanical properties of graphene nanoplatelet/epoxy composites, J. Appl. Polym. Sci. 128 (2013) 4217–4223, https://doi.org/10.1002/app.38645.

[17] L.-C. Tang, Y.-J. Wan, D. Yan, Y.-B. Pei, L. Zhao, Y.-B. Li, L.-B. Wu, J.-X. Jiang, G.-Q. Lai, The effect of graphene dispersion on the mechanical properties of graphene/epoxy composites, Carbon 60 (2013) 16–27, https://doi.org/10.1016/j.carbon.2013.03.050.

[18] Y. Zheng, H. Xu, H. Jing, Q. Ren, Z. Liu, Z. Gao, Q. Ban, Graphene dispersed by pyrene-terminated polyethylene glycol for reinforced epoxy composites, J. Appl. Polym. Sci. 139 (2022) 52110, https://doi.org/10.1002/app.52110.

[19] A. Kumar, S. Li, S. Roy, J.A. King, G.M. Odegard, Fracture properties of nanographene reinforced EPON 862 thermoset polymer system, Compos. Sci. Technol. 114 (2015) 87–93, https://doi.org/10.1016/j.compscitech.2015.04.008.

[20] Z. Yu, L.T. Drzal, Functionalized graphene oxide as coupling agent for graphene nanoplatelet/epoxy composites, Polym. Compos. 41 (2020) 920–929, https://doi.org/10.1002/pc.25423.

[21] M. Alsaadi, B. Younus, A. Erklig, M. Bulut, O. Bozkurt, B. Sulaiman, Effect of graphene nano-platelets on mechanical and impact characteristics of carbon/Kevlar reinforced epoxy hybrid nanocomposites, Proc. IME C J. Mech. Eng. Sci. 235 (2021) 7139–7151, https://doi.org/10.1177/09544062211016883.

[22] A. Khabaz-Aghdam, B. Behjat, E. Marques, R. Carbas, L.F. da Silva, H. Roghani-Mamaqani, Effect of reduced graphene oxide on mechanical behavior of an epoxy adhesive in glassy and rubbery states, J. Compos. Mater. 55 (2021) 3839–3848, https://doi.org/10.1177/00219983211031659.

[23] M.A. Rafiee, J. Rafiee, I. Srivastava, Z. Wang, H. Song, Z.-Z. Yu, N. Koratkar, Fracture and fatigue in graphene nanocomposites, Small 6 (2010) 179–183, https://doi.org/10.1002/smll.200901480.

[24] B. Damirchi, M. Radue, K. Kanhaiya, H. Heinz, G.M. Odegard, A.C.T. van Duin, ReaxFF reactive force field study of polymerization of a polymer matrix in a carbon nanotube-composite system, J. Phys. Chem. C 124 (2020) 20488–20497, https://doi.org/10.1021/acs.jpcc.0c03509.

[25] A. Sarmah, M.A. Morales, A. Srivastava, S. Upama, A. Nandi, T.C. Henry, M. J. Green, A. Vashisth, Interfacial carbon fiber–matrix interactions in thermosetting composites volumetrically cured by electromagnetic fields, Compos. Appl. Sci. Manuf. 164 (2023) 107276, https://doi.org/10.1016/j.compositesa.2022.107276.

[26] Z. Meng, M.A. Bessa, W. Xia, W. Kam Liu, S. Keten, Predicting the macroscopic fracture energy of epoxy resins from atomistic molecular simulations, Macromolecules 49 (2016) 9474–9483, https://doi.org/10.1021/acs.macromol.6b01508.

[27] M. Vassaux, R.C. Sinclair, R.A. Richardson, J.L. Suter, P.V. Coveney, The role of graphene in enhancing the material properties of thermosetting polymers, Advanced Theory and Simulations 2 (2019) 1800168, https://doi.org/10.1002/adts.201800168.

[28] J. Liu, J. Shen, Z. Zheng, Y. Wu, L. Zhang, Revealing the toughening mechanism of graphene–polymer nanocomposite through molecular dynamics simulation, Nanotechnology 26 (2015) 291003, https://doi.org/10.1088/0957-4484/26/29/291003.

[29] X. Zhang, L. Wu, J. Wang, Distinct mechanical properties of polymer/polymer-grafting-graphene nanocomposites, Macromol. Chem. Phys. 219 (2018) 1800161, https://doi.org/10.1002/macp.201800161.

[30] K. Zeng, A. Jibril Ibrahim, Z. Muter Saleh, U.S. Altimari, A. Turki Jalil, M. M. Kadhim, S. Hussain Dilfy, M. Taheri Andani, A. Alizadeh, M. Hekmatifar, Investigation of mechanical and thermal characteristics of epoxy/graphene oxide nanocomposites by molecular dynamics simulation, Mater. Sci. Eng., B 287 (2023) 116087, https://doi.org/10.1016/j.mseb.2022.116087.

[31] C. Lv, Q. Xue, D. Xia, M. Ma, J. Xie, H. Chen, Effect of chemisorption on the interfacial bonding characteristics of Graphene−Polymer composites, J. Phys. Chem. C 114 (2010) 6588–6594, https://doi.org/10.1021/jp100110n.

[32]] Y. Jin, F. Duan, X. Mu, Functionalization enhancement on interfacial shear strength between graphene and polyethylene, Appl. Surf. Sci. 387 (2016) 1100–1109, https://doi.org/10.1016/j.apsusc.2016.07.047.

[33] R. Sun, L. Li, C. Feng, S. Kitipornchai, J. Yang, Tensile property enhancement of defective graphene/epoxy nanocomposite by hydrogen functionalization, Compos. Struct. 224 (2019) 111079, https://doi.org/10.1016/j.compstruct.2019.111079.

[34] Y. Wang, Z. Meng, Mechanical and viscoelastic properties of wrinkled graphene reinforced polymer nanocomposites – effect of interlayer sliding within graphene sheets, Carbon 177 (2021) 128–137, https://doi.org/10.1016/j.carbon.2021.02.071.

[35] The ReaxFF reactive force-field: development, applications and future directions | npj Comput. Mater., (n.d.). https://doi.org/10.1038/npjcompumats.2015.11.

[36] A reactive potential for hydrocarbons with intermolecular interactions | J. Chem. Phys. | AIP Publishing, (n.d.). https://doi.org/10.1063/1.481208.

[37] L. Lindsay, D.A. Broido, Optimized Tersoff and Brenner empirical potential parameters for lattice dynamics and phonon thermal transport in carbon nanotubes and graphene, Phys. Rev. B 81 (2010) 205441, https://doi.org/10.1103/PhysRevB.81.205441.

[38] Y. Shi, A minimalist's reactive potential for efficient molecular modelling of chemistry, Mol. Simulat. 41 (2015) 3–12, https://doi.org/10.1080/08927022.2014.918975.

[39] H. Al Mahmud, M.S. Radue, S. Chinkanjanarot, G.M. Odegard, Multiscale modeling of epoxy-based nanocomposites reinforced with functionalized and non-functionalized graphene nanoplatelets, Polymers 13 (2021) 1958, https://doi.org/10.3390/polym13121958.

[40] J. Cha, J. Kim, S. Ryu, S.H. Hong, Comparison to mechanical properties of epoxy nanocomposites reinforced by functionalized carbon nanotubes and graphene nanoplatelets, Compos. B Eng. 162 (2019) 283–288, https://doi.org/10.1016/j.compositesb.2018.11.011.

[41] J. Sun, C. Wang, J. Yeo, D. Yuan, H. Li, P. Stubbs, C. He, Lignin epoxy composites: preparation, morphology, and mechanical properties, Macromol. Mater. Eng. 301 (2015), https://doi.org/10.1002/mame.201500310 n/a-n/a.

[42] Ultrasonic wave and moduli changes in a curing epoxy resin | Spring, (n.d.). https://doi.org/10.1007/BF02328418.

[43] K. Li, R. Zhao, J. Xia, G.-L. Zhao, Reinforcing microwave absorption MWCNT-epoxy composites using glass fibers for multifunctional applications, Adv. Eng. Mater. 22 (2019), https://doi.org/10.1002/adem.201900780.

[44] M.A. Khan, M.A. Mukaddam, U. Schwingenschlögl, Buckled graphene: a model study based on density functional theory, Chem. Phys. Lett. 498 (2010) 157–161, https://doi.org/10.1016/j.cplett.2010.08.059.

[45] K. Cao, S. Feng, Y. Han, L. Gao, T. Hue Ly, Z. Xu, Y. Lu, Elastic straining of free-standing monolayer graphene, Nat. Commun. 11 (2020) 284, https://doi.org/10.1038/s41467-019-14130-0.

[46] M. Habibur Rahman, S. Mitra, M. Motalab, P. Bose, Investigation on the mechanical properties and fracture phenomenon of silicon doped graphene by molecular dynamics simulation, RSC Adv. 10 (2020) 31318–31332, https://doi.org/10.1039/D0RA06085B.

[47] A.P. Thompson, H.M. Aktulga, R. Berger, D.S. Bolintineanu, W.M. Brown, P. S. Crozier, P.J. in 't Veld, A. Kohlmeyer, S.G. Moore, T.D. Nguyen, R. Shan, M. J. Stevens, J. Tranchida, C. Trott, S.J. Plimpton, Lammps - a flexible simulation tool for particle-based materials modeling at the atomic, meso, and continuum scales, Comput. Phys. Commun. 271 (2022) 108171, https://doi.org/10.1016/j.cpc.2021.108171.

[48] B. Deng, Y. Shi, A reactive coarse-grained model for polydisperse polymers, Polymer 98 (2016) 88–99, https://doi.org/10.1016/j.polymer.2016.06.018.

[49] B. Deng, E.F. Palermo, Y. Shi, Comparison of chain-growth polymerization in solution versus on surface using reactive coarse-grained simulations, Polymer 129 (2017) 105–116, https://doi.org/10.1016/j.polymer.2017.09.048.

[50] B. Deng, L. Huang, Y. Shi, Solvent effect on the diffusion of unentangled linear polymer melts, Langmuir 33 (2017) 11845–11850, https://doi.org/10.1021/acs.langmuir.7b02901.

[51] A. Stukowski, Visualization and analysis of atomistic simulation data with OVITO–the open visualization tool, modelling simul, Mater. Sci. Eng. 18 (2009) 015012, https://doi.org/10.1088/0965-0393/18/1/015012.

[52] P. Malhotra Darshan, A.K. Narula, Studies on the curing kinetics and thermal stability of diglycidyl ether of bisphenol-A using mixture of novel, environment friendly sulphur containing amino acids and 4,4′-diaminodiphenylsulfone, J. Appl. Polym. Sci. 113 (2009) 216–225, https://doi.org/10.1002/app.29798.

[53] R.M. Vinnik, V.A. Roznyatovsky, Kinetic method by using calorimetry to mechanism of epoxy-amine cure reaction, J. Therm. Anal. Calorim. 76 (2004) 285–293, https://doi.org/10.1023/B:JTAN.0000027827.02945.01.

[54] U.Q. Ly, M.-P. Pham, M.J. Marks, T.N. Truong, Density functional theory study of mechanism of epoxy-carboxylic acid curing reaction, J. Comput. Chem. 38 (2017) 1093–1102, https://doi.org/10.1002/jcc.24779.

[55] A. M. Lindrose, Ultrasonic wave and moduli changes in a curing epoxy resin | SpringerLink, (n.d.). https://doi.org/10.1007/BF02328418.].

[56] Y. Shi, Size-dependent mechanical responses of metallic glasses, Int. Mater. Rev. 64 (2019) 163–180, https://doi.org/10.1080/09506608.2018.1476079.

[57] T.L. Anderson, Fracture Mechanics, (n.d.).].

[58] V.M. Nazarychev, A.V. Lyulin, S.V. Larin, A.A. Gurtovenko, J.M. Kenny, S. V. Lyulin, Molecular dynamics simulations of uniaxial deformation of thermoplastic polyimides, Soft Matter 12 (2016) 3972–3981, https://doi.org/10.1039/C6SM00230G.

[59] N. Yousefi, X. Lin, Q. Zheng, X. Shen, J.R. Pothnis, J. Jia, E. Zussman, J.-K. Kim, Simultaneous in situ reduction, self-alignment and covalent bonding in graphene oxide/epoxy composites, Carbon 59 (2013) 406–417, https://doi.org/10.1016/j.carbon.2013.03.034.

[60] Z. Fan, E. Ma, M.L. Falk, Predicting the location of shear band initiation in a metallic glass, Phys. Rev. Mater. 6 (2022) 065602, https://doi.org/10.1103/PhysRevMaterials.6.065602.